Supplemental Material

Electrically tunable single polaritonic quantum dot at room temperature

Hyeongwoo Lee,[1] Ben Whetten,[2] Byong Jae Kim,[3] Ju Young Woo,[4] Yeonjeong Koo,[1] Jinhyuk Bae,[1] Mingu Kang,[1] Taeyoung Moon,[1] Huitae Joo,[1] Sohee Jeong,[3,5] Jaehoon Lim,[3,5] Alexander L. Efros,[6] Markus B. Raschke*,[2] Matthew Pelton*,[7] and Kyoung-Duck Park*[1]

[1]*Department of Physics, Pohang University of Science and Technology (POSTECH), Pohang 37673, Republic of Korea*

[2]*Department of Physics and JILA, University of Colorado, Boulder, CO 80309, United States*

[3]*Department of Energy Science, Center for Artificial Atoms, Sungkyunkwan University (SKKU), Suwon 16419, Republic of Korea*

[4]*Digital Transformation R&D Department, Korea Institute of Industrial Technology (KITECH), Ansan 15588, South Korea*

[5]*SKKU Institute of Energy Science and Technology (SIEST), Sungkyunkwan University (SKKU), Suwon 16419, Republic of Korea*

[6]*Naval Research Laboratory, Washington, DC 20375, United States*

[7]*Department of Physics, University of Maryland, Baltimore County (UMBC), Baltimore, MD 21250, United States*

S1. Experimental methods

S1.1 Synthesis of CdSe/$Zn_{1-x}Cd_xS$ QDs.

Chemicals. Cadmium oxide (CdO, 99.95%), 1- octadecene (ODE, 90%), trioctylphosphine (TOP, 97%) and 1-dodecanethiol (DDT, 98%) were purchased from Alfa Aesar. Oleic acid (OA, 90%), selenium (99.998%), sulfur (99%), zinc acetate [$Zn(Ac)_2$] were purchased from Sigma-Aldrich. All chemicals were used as received.

Stock solutions. Cadmium oleate [$Cd(OA)_2$] and zinc oleate [$Zn(OA)_2$] stock solutions were prepared by reacting 20 mmol of CdO or 20 mmol $Zn(Ac)_2$ with 20 mL of OA and 20 mL ODE at 120 ◦C under vacuum. Trioctylphosphine selenide (TOPSe) and trioctylphosphine sulfide (TOPS) stock solutions were synthesized by reacting 10 mmol of Se or S with 5 mL TOP under inert atmosphere.

Synthesis of CdSe core. Wurtzite CdSe cores with a diameter of 5.1 nm were prepared. CdSe seed was first prepared by rapidly introducing 0.2 mL TOPSe to the mixture of 0.2 mL of $Cd(OA)_2$ and 12 mL of ODE at 300 ◦C. After 30 s, 2 mL of TOP was slowly added to the reaction. To grow CdSe seed to 5.1 nm, a mixture of 1 mL TOPSe, 4 mL $Cd(OA)_2$ and 3 mL ODE was immediately injected to the reaction at a rate of 10 mL/hr for 1.4 mL and 14 mL/hr for the remaining 3.2 mL. The diameter of CdSe the cores was estimated from the first exciton peak using a sizing curve.

Synthesis of CdSe/$Zn_{1-x}Cd_xS$ QDs. Without purification, we added 2 mL of $Cd(OA)_2$ and slowly added 0.4 mL of DDT dropwise for 30 s. The growth of the CdS shells was completed after 30 min. To overgrow the CdZnS shells, without purification, we first added 6 mL of $Zn(OA)_2$ and 1.5 mL of TOPS, then slowly injected 2 mL of $Cd(OA)_2$ for 2 min. After 7 min, we performed the same procedure once again. At the end of the reaction, the reactor was quenched to room temperature. The fabricated QDs were purified five times by precipitation and redispersion procedure using ethanol and toluene and dispersed in hexane for spectroscopic study.

S1.2. *e*-TESC spectroscopy setup.

The CdSe/$Zn_{1-x}Cd_xS$ QDs were spin-coated onto a template-stripped Au substrate and loaded on a piezo-electric transducer (PZT, P-611.3X, Physik Instrumente) for XY scanning and atomic force feedback with <0.1 nm positioning precision. To facilitate the formation of a nanoplasmonic tip-cavity, an Au tip with a radius of curvature of ∼15 nm was used. The Au tip, which is fabricated with a refined electrochemical etching protocol, was attached to a quartz tuning fork (resonance frequency of 32.768 kHz) to regulate the distance between the tip and sample based on shear-force AFM operated by a digital AFM controller (R9+, RHK Technology).

For the *e*-TESC experiments, a conventional optical spectroscopy setup was combined with home-built shear-force AFM. For a high-quality wavefront of the excitation beam, a He-Ne laser (594 nm, <0.5 mW) was coupled and passed through a single-mode fiber and collimated again using an aspheric lens. The collimated beam was then passed through a half-wave plate to make the excitation polarization parallel with respect to the tip axis. Finally, the beam was focused onto the Au tip using a microscope objective (NA = 0.8, LMPLFLN100X, Olympus) with a side illumination geometry. To ensure highly efficient laser coupling to the Au tip, the tip position was controlled with ∼30 nm precision by Picomotor actuators (9062-XYZ-PPP-M,

Newport). TEPL responses were collected using the same microscope objective (backscattering geometry) and passed through an edge filter (LP02-633RE-25, Semrock) to cut off the fundamental laser line. TEPL signals were then dispersed onto a spectrometer (f = 328 mm, Kymera 328i, Andor) and imaged with a thermoelectrically cooled charge-coupled device (CCD, iDus 420, Andor) to obtain the TEPL spectra. In our measurements, TEPL spectra were collected with an exposure time of 0.5 s. For the electric-field module, the tip and sample were electrically connected to a function generator. By applying a potential difference between the tip and sample, a localized electric field was induced between the tip and sample. To read the tunneling current, we used the STM module (R9+, RHK Techonolgy).

S2. Structural characterization of plasmonic Au tip.

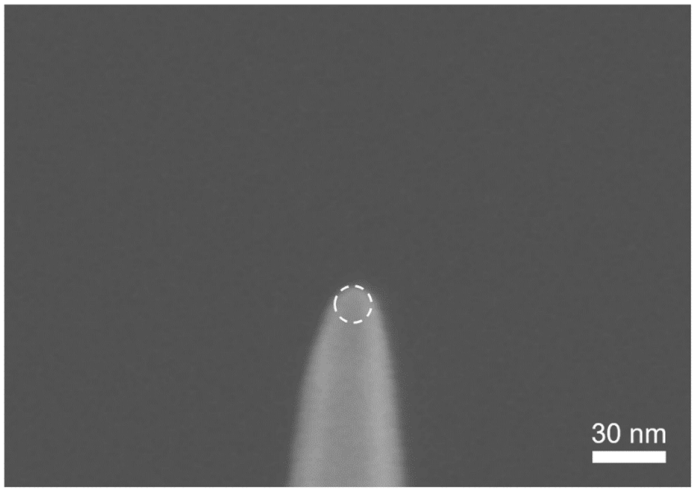

Fig. S2. SEM image of plasmonic Au tip with radius of curvature of ~15 nm.

S3. Structural characterization of synthesized CdSe/$Zn_{1-x}Cd_xS$ QDs.

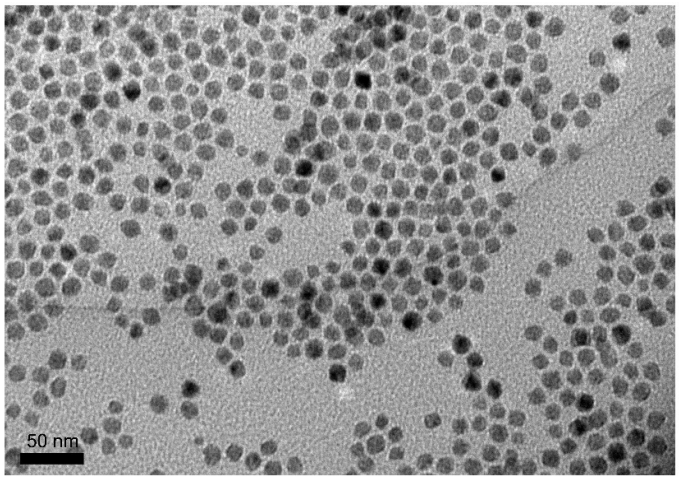

Fig. S3. Transmission electron microscopy (TEM) image of CdSe/$Zn_{1-x}Cd_xS$ QDs transferred onto TEM grid.

S4. Optical characterization of synthesized CdSe/$Zn_{1-x}Cd_xS$ QDs.

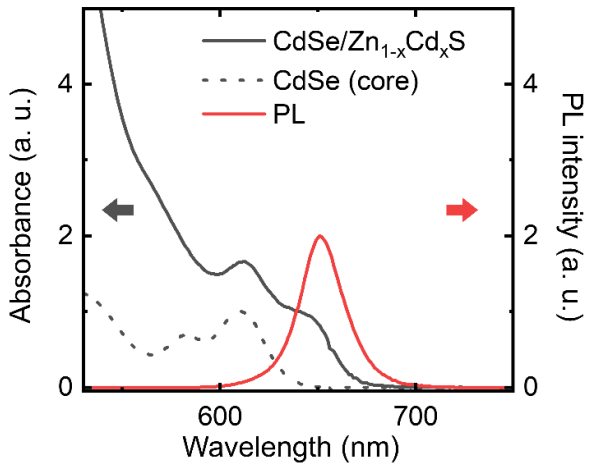

Fig. S4. Absorption spectra of CdSe core (black dashed line) and CdSe/$Zn_{1-x}Cd_xS$ QDs (black line). PL spectrum of CdSe/$Zn_{1-x}Cd_xS$ QDs (red line). These data are obtained in the solution phase before spin-coating the QDs on an Au substrate.

S5. Emission of CdSe/$Zn_{1-x}Cd_xS$ QDs in different substrates.

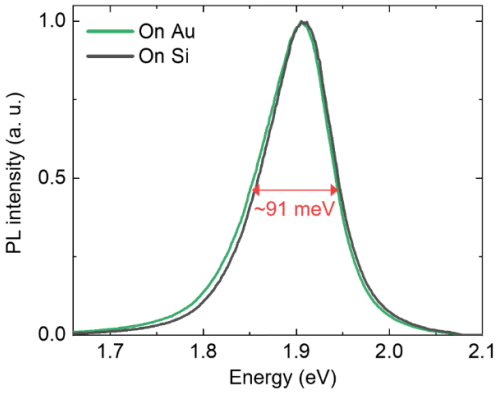

Fig. S5. Far-field micro-photoluminescence spectra of CdSe/$Zn_{1-x}Cd_xS$ QDs spin-coated on Au (green) and Si (black).

S6. Confirming single level density of spin-coated $CdSe/Zn_{1-x}Cd_xS$ QDs.

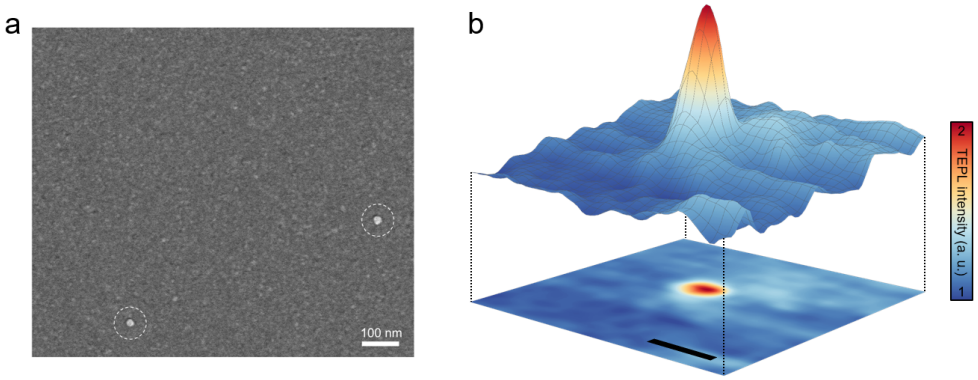

Fig. S6. (a) Scanning electron microscopy (SEM) image of $CdSe/Zn_{1-x}Cd_xS$ QDs, spin-coated on templated stripped Au substrate and covered by Al_2O_3 capping layer of ~0.5 nm. (b) TEPL image of a single $CdSe/Zn_{1-x}Cd_xS$ QD. The scale bar is 100 nm.

S7. Shear-force atomic force microscopy with electric-field control.

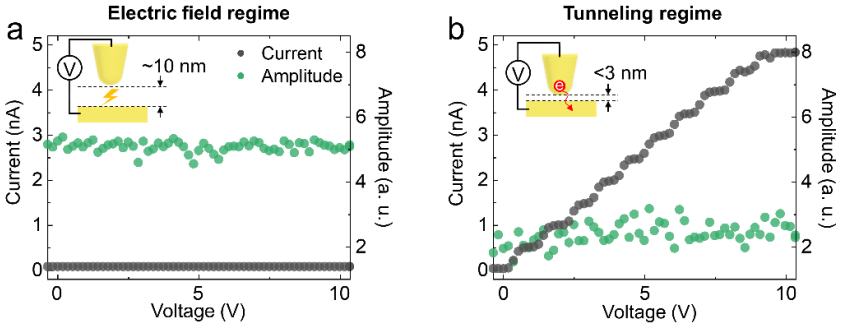

Fig. S7. I-V curve for the electric field regime (a) and tunneling regime (b).

Shear-force atomic force microscopy enables to control tip-sample distance with <0.2 nm precision and <0.1 nm fluctuation. Therefore, we can switch between two regimes: electric field regime and tunneling regime. In the electric field regime, the tip-substrate distance is considered as larger than tunneling threshold, leading to generate potential difference between the tip and sample. It induces the local electric field with the maximum strength of ~10 V/nm. Fig. S7a shows the I-V curve for the electric field regime where tip-sample distance >10 nm. Although applying tip-sample bias, current cannot be induced. By contrast, when we decrease the setpoint of feedback amplitude, the tip-substrate distance is correspondingly decreased and within the tunneling threshold, i.e., <3 nm, facilitating charge flows through the gap between the tip and substrate. Fig. S7b shows the I-V curve for the tunneling regime. The decreased feedback amplitude compared to Fig. S7a well demonstrates the decrease in tip-substrate distance. In addition, the current increases proportional to the applied external electric field due to the charge tunneling. We note that this measurement is conducted on the bare Au substrate without QDs to independently characterize the electrical capabilities of *e*-TESC spectroscopy.

S8. Energy variation of individual QDs.

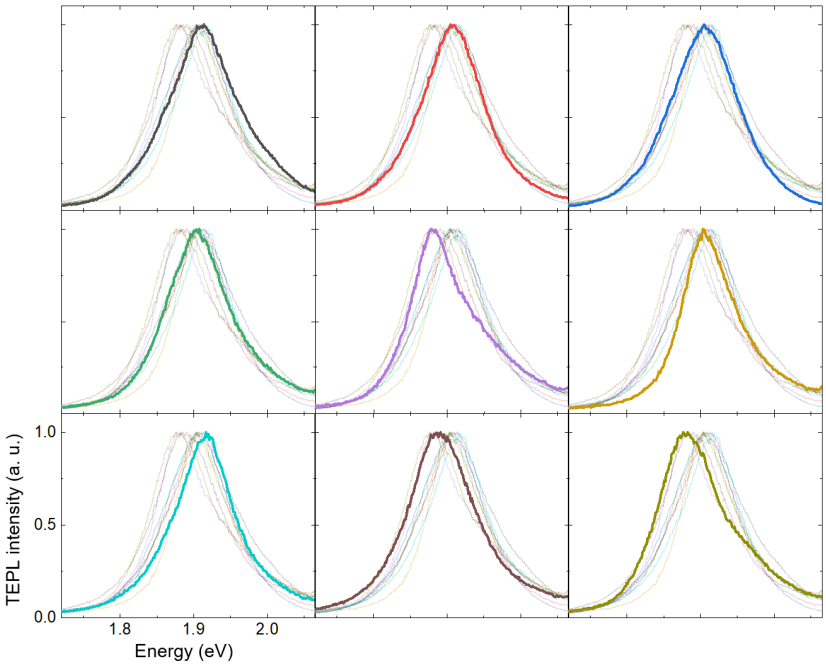

Fig. S8. TEPL spectra of 9 QDs weakly coupled to tip-induced plasmonic cavity, exhibiting their energy variation with a range of ~30 meV. Here, the tip-QD distance is maintained >5 nm to induce weak coupling.

S9. QD energy detuning and plexciton energy.

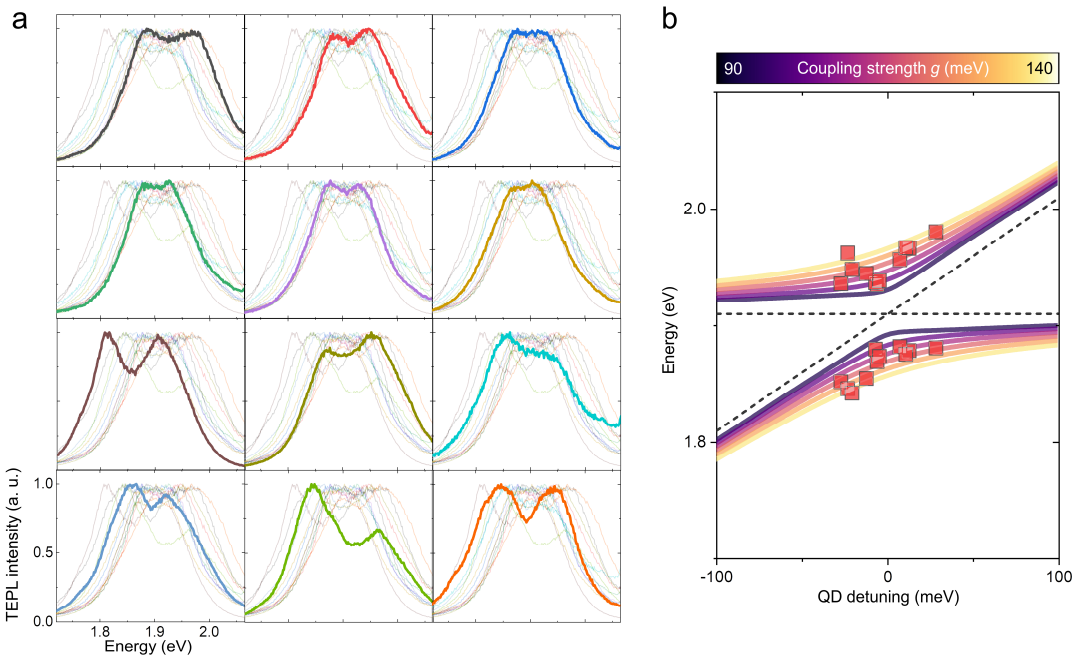

Fig. S9. (a) TEPL spectra of 12 QDs strongly coupled to tip-induced plasmonic cavity. (b) Corresponding polariton energies as function of extracted detuning value, derived from (a).

In Fig. S8, the individual QDs exhibits variations in their emission energy with a range of ~30 meV. This energy variations can lead to the QD energy detuning and consequently affect to the plexcitonic states. Fig. S9a shows the plexcitonic emission spectra of 12 QDs when the tip-QD distance is <3 nm. Because we fix the plasmonic mode volume, these changes in emission can be attributed to the variations in excitonic components. When we plot polariton energies and anticrossing curves for TEPL spectra of 12 QDs, the variations in QD energy are observed, as shown in Fig. S9b. The range of derived QD energy detuning has a comparable range to the energy variations observed in Fig. S8. The variations in coupling strength can be demonstrated with the different orientations of transition dipole moments in QDs [1].

S10. Spatial positioning of electric-field nanoplasmonic tip-cavity.

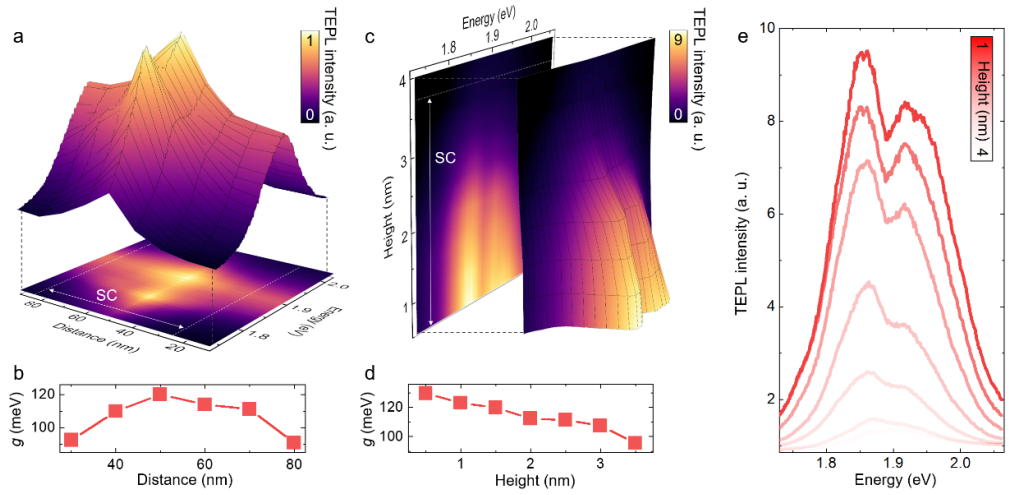

Fig. S10. Spatial dependent TEPL spectra and corresponding coupling strength with lateral (a, b) and vertical (c, d) plasmonic tip control. (e) Distance-dependent TEPL spectra, derived from Fig. S10c.

To confirm the mechanical tunability of e-TESC and its effect on the plexcitonic states, i.e., control of the cavity mode volume, we move the plasmonic tip three-dimensionally on the single isolated QD, resulting in coupling strength modification. We systematically move the tip position in lateral and vertical direction to control plasmonic cavity mode volume. When the QD is in resonance with the cavity mode, the plexcitonic emission with Rabi splitting is observed (strong coupling), whereas the increase in spontaneous emission rate without noticeable spectral changes is observed in the off-resonance condition (weak coupling). We then obtain hyperspectral TEPL spectra as the plasmonic tip laterally crosses the QD. The continuous change in Rabi splitting energy, with the maximum difference of ~93 meV at the top position of QD, is observed with correspondingly changing coupling strength, as shown in Fig. S10a and b. We then move the plasmonic tip into the strongest coupling position, i.e., top of the QD, and vertically retract the plasmonic tip. As expected, gradual decrease in Rabi splitting and coupling strength is observed as the cavity mode volume decreases, as shown in Fig. S10c-e.

S11. Dipole orientation dependent coupling strength

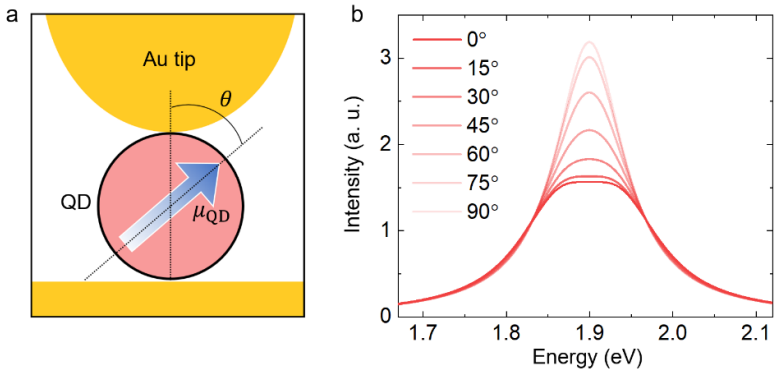

Fig. S11. (a) Illustration of single QD with transition dipole moment μ_{QD}, confined in the tip-induced nanoplasmonic cavity. Relative angle between oscillation axis of tip plasmon and transition dipole moment is θ. (b) Plexciton spectra with different θ. Other fitting parameters ω_{QD}, ω_{SP}, γ_{QD}, γ_{SP}, and g are fixed to 1.9 eV, 1.9 eV, 0.1 eV, 0.15 eV, 0.08 eV respectively.

The axis mismatch between the transition dipole moment of QDs and the polarization of the confined plasmon mode reduces the effective coupling strength, as shown in Fig. S11a-b. For a QD with its maximum coupling strength of 0.080 eV, 45 ° of dipole misorientation results in a decrease of the coupling strength to ~0.057 eV. This low coupling strength at zero leads to greater uncertainty in the fitted coupling strength.

S12. Experimental threshold bias in controlling plexcitonic states.

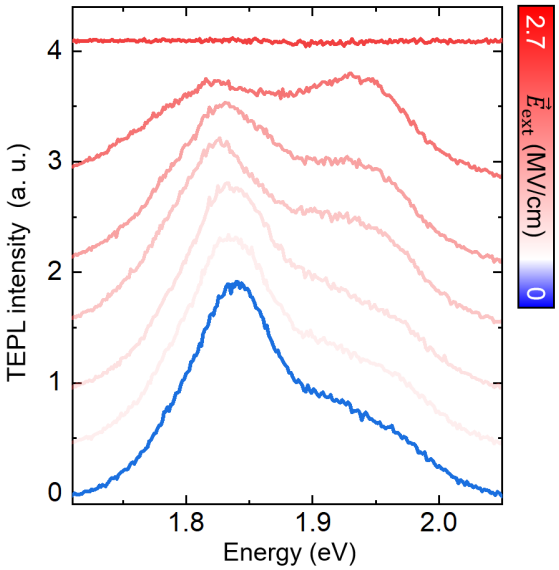

Fig. S12. TEPL spectra of a single QD strongly coupled to cavity plasmon as function of external electric bias.

To investigate the threshold bias of electrically tunable plexcitonic states, we continuously increase the external electric field. Fig. S12 shows the continuously increased Rabi splitting with increased external electric field. At ~2.69 MV/cm, TEPL emission from the QD suddenly starts to decrease and finally disappears, attributed to the electric field induced dielectric breakdown [2, 3]. Therefore, in the main experiment, we strictly limit switching bias to ~1.15 MV/cm, which sufficiently guarantees the high stability and repeatability.

S13. Effect of external electric field on plasmon response.

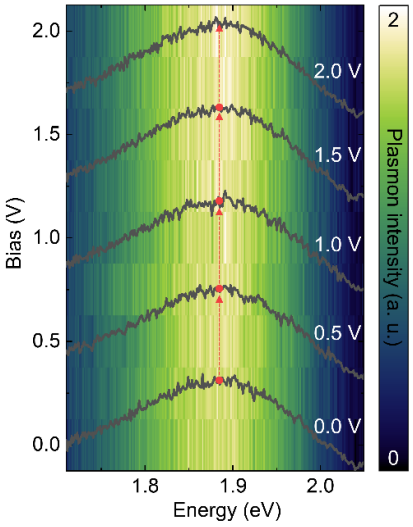

Fig. S13. TEPL spectra of tip-induced cavity plasmon as function of external electric bias.

To exclude the effect of plasmonic components during the electrical control of plexcitonic states, i.e., to fix the plasmonic parameters, we first induce the cavity plasmon by approaching plasmonic Au tip to the bare Si-template stripped Au substrate without QDs sample. Here, we exploit the gold photoluminescence, most likely involves transitions between states near the conduction-band edge and in the lower-lying d-band, as its spectral shape indicates the plasmon resonance [4]. In our geometry, the gold photoluminescence can be amplified resonantly by plasmonic enhancement [5, 6, 7]. We then apply the external electric field and observe TEPL spectra of cavity plasmon, as shown in Fig. S13. The noticeable changes in plasmon emission, such as energy and linewidth, are not observed. Note that the TEPL spectra of tip-induced cavity plasmon are measured at electric field regime.

S14. Mechanical stability and reproducibility of *e*-TESC platform

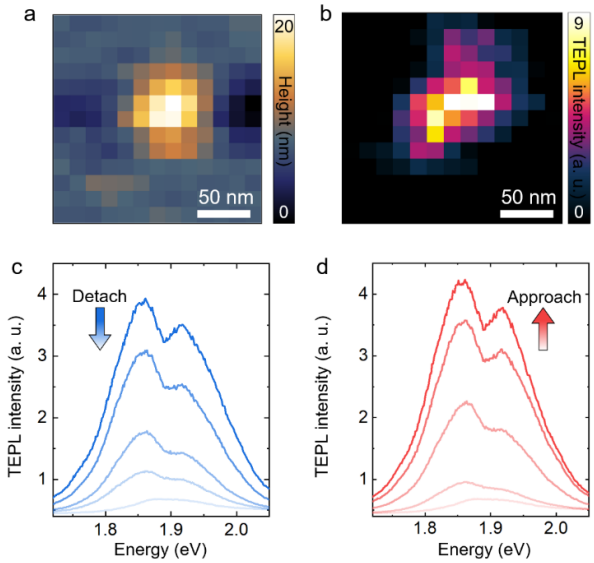

Fig. S14. Topography (a) and TEPL (b) images of a single-isolated QD in weak coupling regime. TEPL spectra as plasmonic tip is detached from QD (c) and again approached to QD.

The *e*-TESC spectroscopy, based on shear-force AFM can facilitate sub-diffraction-limited optical detection of a single-isolated QD with the spatial resolution of ~15 nm, as shown in Fig. S14a-b. This allows us to precisely locate the plasmonic tip immediately on the QD in a reversible manner. Fig. S14c-d show the TEPL spectra of strongly coupled QD as the plasmonic tip removed from the QD (Fig. S14c) and again approached to the QD (Fig. S14d), indicating the reversibility and stability of the system.

S15. Electrical stability and reproducibility of *e*-TESC platform

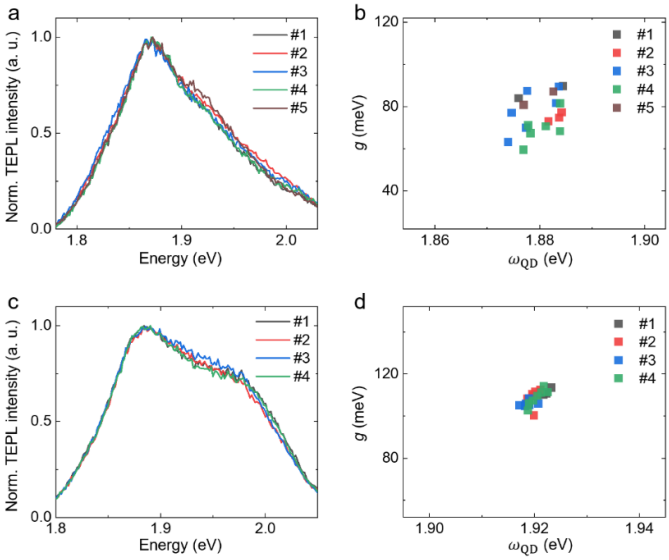

Fig. S15. TEPL spectra (a) and plexciton parameters (b) with iterative electrical modulation, derived from Fig. 1f. TEPL spectra (c) and plexciton parameters (d) with iterative electrical modulation, derived from Fig. 1j.

To investigate the possible irreversible changes from electrical modulation, we compare TEPL spectra, each obtained after one cycle of the electrical modulation. As shown in Fig. S15a-b, TEPL spectra show negligible changes after five iterations of electrical modulation. Correspondingly, the derived coupling strengths and QD energies exhibit insignificant changes, residing within the error ranges. Similarly, Fig. S15c-d show the negligible changes with repeated electrical modulation. Note that the larger range of distribution in Fig. S15b compared to Fig. S15d can be attributed to the fitting uncertainty from the lower coupling strength.

S16. Mechanical switching between week and strong coupling regime

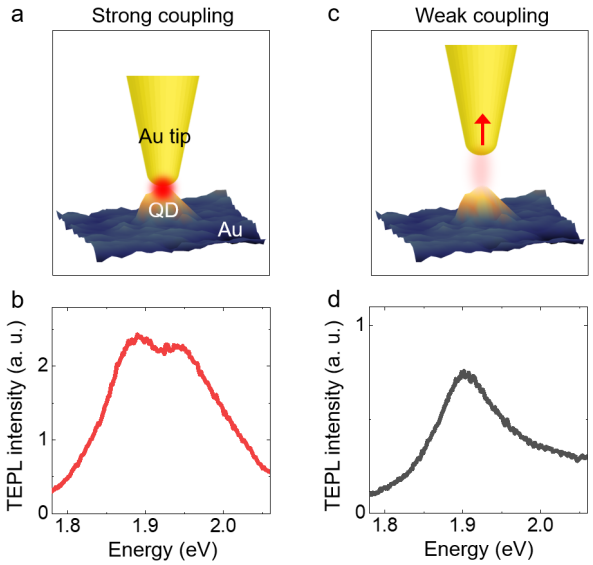

Fig. S16. TEPL spectra of strongly coupled (a, b) and weakly coupled (c, d) QDs.

By adjusting the distance between the tip and sample, we stably switch the states between the strong coupling and weak coupling regime in a reversible manner. When the tip-QD distance is less than 3 nm, the strongly coupled QD exhibits dramatically changed its emission spectrum, as shown in Fig. S16a-b. By contrast, with the tip-QD distance is greater than 10 nm, the interaction between the plasmons and excitons are sufficiently minimized owing to the largely increased cavity mode volume. In this weak coupling regime, QD emission shows negligible changes in its emission spectrum compared to uncoupled QDs, as shown in Fig. S16c-d.

S17. Quantum confined Stark effect of QDs in week coupling regime

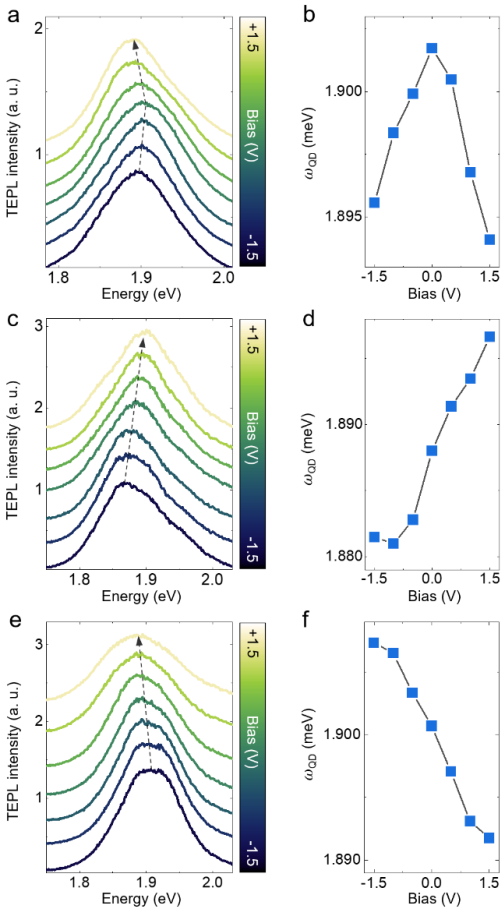

Fig. S17. Electrical control of single QDs emission in weak coupling regime. TEPL spectra as a function of external electric bias with derived emission resonance for $\vec{E}_{\mathrm{q}} \approx 0$ (a, b), upward $\vec{E}_{\mathrm{q}}^{+}$ (c, d), and downward $\vec{E}_{\mathrm{q}}^{-}$ (e, f).

To investigate QCSE of single QDs while minimizing the interaction with plasmons, we increase the tip-QD distance until the QD is sufficiently in the weak coupling regime. As a result, we observe representative QCSE behaviors with different built-in electric field $\vec{E}_{\mathrm{built}}$. Without built-in electric field, i.e., $\vec{E}_{\mathrm{q}} \approx 0$, the TEPL spectra exhibit the decrease in emission energy for both directions of external electric field, as shown in Fig. S17a-b. For upward built-in electric field $\vec{E}_{\mathrm{q}}^{+}$, emission energy increases as a function of the external electric bias, as shown in Fig. S17c-d. By contrast, for downward built-in electric field $\vec{E}_{\mathrm{q}}^{-}$, the opposite behavior is observed, i.e., decrease in emission energy as a function of external electric bias (Fig. S17e-f). Fitting QCSE results to Eq. (3) in the main text leads to $\vec{V}_{\mathrm{q}} \approx 0.141$ V, $\vec{V}_{\mathrm{q}}^{+} \approx 2.825$ V, and $\vec{V}_{\mathrm{q}}^{-} \approx -2.431$ V, with required surface charges of ~0.08 e, ~1.45 e, and ~1.24 e, respectively. The range of fitting parameters in the weak coupling regime well corresponds to the one from the strong coupling regime.

S18. Theoretical analysis of electrically tunable plexcitonic states.

In order to obtain analytical estimates for the quantum-confined Stark shift within a CdSe/CdS core/shell nanocrystal, we approximate the nanocrystal as being spherical, take the DC dielectric constants of CdSe and CdS to be approximately equal, and assume that the electron and hole wavefunctions are entirely localized within the CdSe core. The confining potentials for carriers within the cores are assumed to be parabolic. This highly simplified model is intended only to provide insight into the functional dependence and order of magnitude for the electric-field induced change in quantum-dot transition frequency, ω_{QD}, and coupling strength, g. Quantitative modeling would require numerical treatment and is outside of the scope of the current manuscript.

For an applied external electric field $\vec{E}_{\mathrm{ext}}$, the electric field inside the nanocrystal is $E_{\mathrm{s}} = [3/(\varepsilon+2)]E_{\mathrm{ext}}$, where ε is the dielectric constant inside the nanocrystal, and the dielectric constant of the surroundings is taken to be unity. This electric field creates the potential

$$V = E_{\mathrm{s}}\cos\theta r. \tag{1}$$

First-order changes to the electron and hole wavefunction energies cancel out in the approximation of parabolic potentials, because the wave functions of electrons and holes are identical. Second-order changes have contributions from both the valence and conduction bands. However, both of these contributions have the same sign, and the main contribution comes from the hole, because of its larger effective mass [8]. This contribution can be estimated as

$$\Delta E_{ex} = \frac{|\langle 1P_{\mathrm{e}}|V|1S_{\mathrm{e}}\rangle|^2}{-\Delta E_{\mathrm{e}}^{\mathrm{PS}}} + \frac{|\langle 1P_{\mathrm{h}}|V|1S_{\mathrm{h}}\rangle|^2}{-\Delta E_{\mathrm{h}}^{\mathrm{PS}}}, \tag{2}$$

where $|1S_{\mathrm{e}}\rangle$ and $|1P_{\mathrm{e}}\rangle$ designate the 1*S* and *1P* wavefunctions for the electron, respectively, ΔE_3^{PS} is the difference in energy between these two wavefunctions, and similarly for the hole.

From this, we obtain the quantum-confined Stark shift:

$$\Delta E_{\mathrm{ex}} = -|\langle 1\mathrm{P_e}|\mathrm{V}|1\mathrm{S_e}\rangle|^2 \frac{2a^2}{\hbar^2(4.49^2-\pi^2)}(m_{\mathrm{e}}+m_{\mathrm{h}}), \tag{3}$$

where we use the fact that square of the matrix elements for electron and holes $|\langle 1P_{\mathrm{e}}|V|1S_{\mathrm{e}}\rangle|^2 = |\langle 1P_{\mathrm{e}}|V|1S_{\mathrm{e}}\rangle|^2$ are equal to each other, and electron and hole energy levels $E_{1\mathrm{S}}^{(\mathrm{e,h})} \approx \hbar^2\pi^2/2\mathrm{m}_{(\mathrm{e,h})}a^2$ and $E_{1\mathrm{P}}^{(\mathrm{e,h})} \approx \hbar^2(4.49)^2/2\mathrm{m}_{(\mathrm{e,h})}a^2$ where m_{e} and m_{h} are the electron and hole effective masses correspondingly, and a is the radius of the core. To calculate the matrix element, we need the wave function of $1S$ electron level:

$$\psi_{1S}(r) = \frac{1}{\sqrt{2\pi a r}} sin\left(\frac{\pi r}{a}\right),\ \psi_{1P,m=0}(r) = \sqrt{\frac{3}{4\pi}} cos\theta R_1(r),\ R_1 = \frac{b}{a^{3/2}} j_1(4.49r/a) \tag{4}$$

where $j_1(x)$ is the spherical Bessel function and the coefficient b is determined from normalization condition $\int_0^a r^2 dr[R_1(r)]^2 = 1$:

$$b = 1/\sqrt{\int_0^1 x^2 dx j_1^2(4.49x)}\,. \tag{5}$$

Integration of the matrix element $\langle 1\mathrm{P}_e|\mathrm{V}|1\mathrm{S}_e\rangle$ over θ gives $2/3$ and integration over ϕ gives 2π. The rest can be written as:

$$\langle 1P|V|1S\rangle = \frac{4\pi}{3} eE_s \int_0^{a_c} drr^2 \psi_{1S}(r) \sqrt{\frac{3}{4\pi}} R_1(r) r = \sqrt{\frac{2}{3}} bc[eE_s a]. \quad (6)$$

where

$$c = \int_0^1 x^2 dx j_1(4.49x) sin(\pi x). \quad (7)$$

The transition dipole moment μ, by contrast, is proportional to the overlap integral between the electron and hole within the wave function of a confined exciton $\Psi_{\mathrm{ex}}(\boldsymbol{r}_{\mathrm{e}}, \boldsymbol{r}_{\mathrm{h}})$ [9-11]:

$$\mu \propto K = |\int d^3 r_{\mathrm{e}} d^3 r_{\mathrm{h}} \Psi_{\mathrm{ex}}(\boldsymbol{r}_{\mathrm{e}}, \boldsymbol{r}_{\mathrm{h}}) \delta(\boldsymbol{r}_{\mathrm{e}} - \boldsymbol{r}_{\mathrm{h}})|^2. \quad (8)$$

The electric field affects the wave function of the exciton ground state by mixing it with the wave functions of upper exciton states with different symmetry. We can estimate this change by assuming that the exciton is in the strong confinement regime [12], so that the exciton function $\Psi_{\mathrm{ex}}(\boldsymbol{r}_{\mathbf{e}}, \boldsymbol{r}_{\mathrm{h}}) = \psi_{\mathrm{e}}(\boldsymbol{r}_{\mathrm{e}}) \psi_{\mathrm{h}}(\boldsymbol{r}_{\mathrm{h}})$, where $\psi_{\mathrm{e}}(\boldsymbol{r}_{\mathrm{e}})$ and $\psi_{\mathrm{h}}(\boldsymbol{r}_{\mathrm{h}})$ are the wave functions of confined electrons and holes, respectively.

For sufficiently small electric field, so that the electric field energy $eE_{\mathrm{s}}a$ is much smaller than the energy between $1P_{\mathrm{e}}$ and $1S_{\mathrm{e}}$ levels, one can neglect the mixing for the electron wave function and take into account only the mixing for the hole levels. The wave function of the hole in the external electric field $|1S(E)\rangle_{\mathrm{h}}$ can be written as:

$$|1S(E)\rangle_{\mathrm{h}} = \left[|1S\rangle_{\mathrm{h}} + \frac{\langle 1P_{\mathrm{h}}|V|1S_{\mathrm{h}}\rangle}{\Delta E_{\mathrm{h}}^{\mathrm{PS}}} |1P\rangle_{\mathrm{h}} \right] N(E) \ , \quad (9)$$

where the square of the normalization constant $N(E)$ is

$$N^2(E) = \frac{1}{1 + |\langle 1P_{\mathrm{h}}|V_{\mathrm{E}}|1S_{\mathrm{h}}\rangle|^2 / (\Delta E_{\mathrm{h}}^{\mathrm{PS}})^2}. \quad (10)$$

This gives the square of overlap integral:

$$K = \left| \int d^3 r |1S(r)\rangle_{\mathrm{e}} |1S(E)(r)\rangle_{\mathrm{h}} \right|^2 = N^2(E). \quad (11)$$

Using Eq. (6),

$$\left| \langle 1P \,|\, V \,|\, 1S \rangle \right|^2 = \frac{2}{3} b^2 c^2 [eE_s a]^2 \ , \quad (12)$$

and in the parabolic band approximation:

$$\Delta E_{\mathrm{h}}^{\mathrm{PS}} = \frac{\hbar^2}{2 m_{\mathrm{h}} a^2} (4.49^2 - \pi^2). \quad (13)$$

This expression requires a knowledge of hole effective mass, and in principle we could use the value of the heavy hole mass in CdSe. However, it may be more reasonable to use for the estimation of $\Delta E_{\mathrm{h}}^{\mathrm{PS}}$, the distance between $1P_{3/2}$ and $1S_{3/2}$ hole levels [13].

For a coupled QD cavity system, the coupling strength is

$$g = 2\sqrt{\Omega_o^2 - \frac{(\omega_{\mathrm{QD}} - \omega_{\mathrm{SP}})^2}{4} + \frac{(\gamma_{\mathrm{SP}} - \gamma_{\mathrm{QD}})^2}{16}}, \tag{14}$$

where Ω_o, ω_{QD}, ω_{SP}, γ_{QD}, and γ_{SP} denote vacuum Rabi frequency, the resonance frequency of QD, the resonance frequency of plasmon, the decay rate of QD, and the decay rate of plasmon, respectively. Using $\Omega_o \propto \mu \propto K$, and Eqs. (3), (10), and (11), we can write

$$g = 2\sqrt{\left(\frac{\Omega_0}{1 + \left(\frac{|\langle 1P_{\mathrm{h}}|V|1S_{\mathrm{h}}\rangle|}{\Delta E_{\mathrm{h}}^{\mathrm{PS}}}\right)^2}\right)^2 - \frac{(\omega_0 - S|\langle 1P_{\mathrm{h}}|V|1S_{\mathrm{h}}\rangle|^2)^2}{4}} + \gamma_0\,, \tag{15}$$

where $\omega_0 = \omega_{\mathrm{QD}} - \omega_{\mathrm{SP}}$, $\gamma_0 = (\gamma_{\mathrm{SP}} - \gamma_{\mathrm{QD}})^2/16$, and S is the Stark shift per volt squared (obtained from Eqs. (3) and (6)).

For a uniform applied external field, the potential in Eq. (15) is given by Eq. (1). If there is also a potential due to a charge on the surface of the QD, that additional built-in potential is given by [14]

$$V(\boldsymbol{r}, a) = \frac{e^2}{k_s|\boldsymbol{r} - \boldsymbol{a}|} + \frac{e^2}{k_s a}\sum_{k=0}^{\infty} B_k \left(\frac{r}{a_s}\right)^k P_k(cos\theta)\,, \tag{16}$$

where e is the electric charge, $\boldsymbol{r}$ is the coordinate, θ is the angle between the charge direction and $\boldsymbol{r}$, a is the radius of the QD (including shell), P_{k} is the Legendre polynomial, and the coefficients in the sum are

$$B_k = \frac{(\varepsilon - 1)(k + 1)}{\varepsilon k + k + 1}, \tag{17}$$

We can write

$$\frac{1}{|\boldsymbol{r} - \boldsymbol{a}|} = \frac{1}{a} + P_1(cos\theta)\frac{r}{a^2} + P_2(cos\theta)\frac{r^2}{a^3} + \cdots. \tag{18}$$

Only terms proportional to $P_1(cos\theta) = cos\theta$ contributed to the matrix elements $\langle 1P|V|1S\rangle$. Integration over θ in the matrix element is $\int \sin\theta d\theta \cos^2(\theta) = 2/3$. This results in the matrix element

$$\langle 1P|V|1S\rangle = \frac{4\pi}{3}\frac{e^2}{\varepsilon_s a}\int_0^a drr^2\psi_{1S}(r)\sqrt{\frac{3}{4\pi}}R_1(r)\frac{r}{a}[1 + B_1] = \sqrt{\frac{2}{3}}bc(1 + B_1)\frac{e^2}{\varepsilon_s a} \tag{19}$$

where $B_1 = 2(\varepsilon - 1)/(\varepsilon + 2)$.

Substituting Eq. (19) into Eq. (3) gives the Stark shift for a single charge on the QD surface. Equivalently, it can be used to estimate the number of surface charges required to produce a given Stark shift. This shift due to the built-in dipole moment will combine with the shift due to the applied field, producing an offset in the parabolic relationship between applied field and QD transition energy.

S19. Theoretical estimation of quantum confined Stark effect.

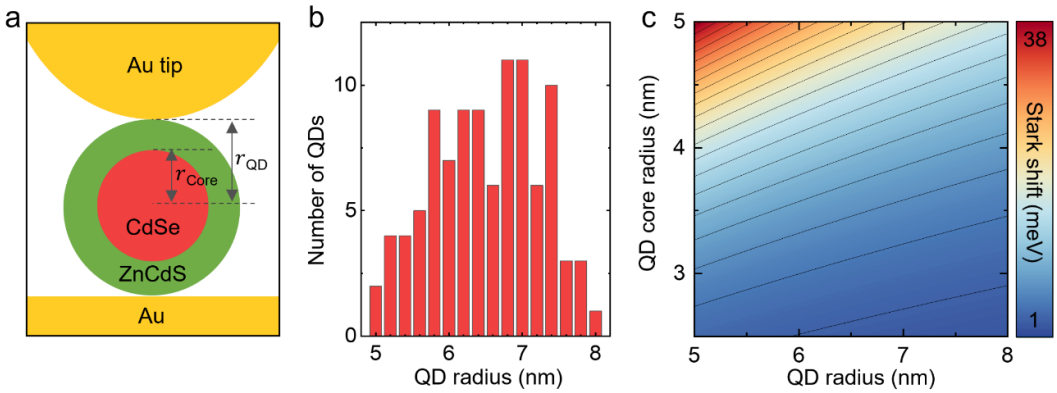

Fig. S19. (a) Illustration of QD geometry with core radius r_{core} and QD radius r_{QD}, confined in electric-field nanoplasmonic cavity. (b) Size histogram for 100 QDs, derived from TEM image in Fig. S2. (c) Calculated Stark shift as function of QD geometry under external bias of 1 V.

To estimate the Stark shift of QDs confined in the electric-field nanoplasmonic cavity, we calculate the Stark shift with different QD core size and shell thickness. Note that we assume the position of plasmonic Au tip to be immediately above a QD to reflect the experimental conditions (Fig. S19a), i.e., decrease in shell thickness indicates the increase in external electric field. From TEM images, we obtain the distribution of QD size, indicating average QD radius of ~6.5 nm, as shown in Fig. S19b. Fig. S19c shows the theoretical Stark shift with different QD core size and shell thickness. The increase in QD core size results in correspondingly increased Stark shift, which is in good agreement with previous study [15]. Decreasing the QD radius with fixed core size allows us to investigate the effect of shell thickness. Decreased shell thickness enables the tip to be closer to the Au substrate and induce higher external electric field, consequently leading to the increased Stark shift.

While the thinner shell thickness can lead to the larger Stark shift, it leads to the reduced fluorescence quantum yield, magnitude of the built-in field, and stability under ambient conditions [16, 17]. We optimize the QD core size and shell thickness to maximize the Stark shift while considering these factors.

S20. Role of built-in electric field in electrically tunable plexcitonic states.

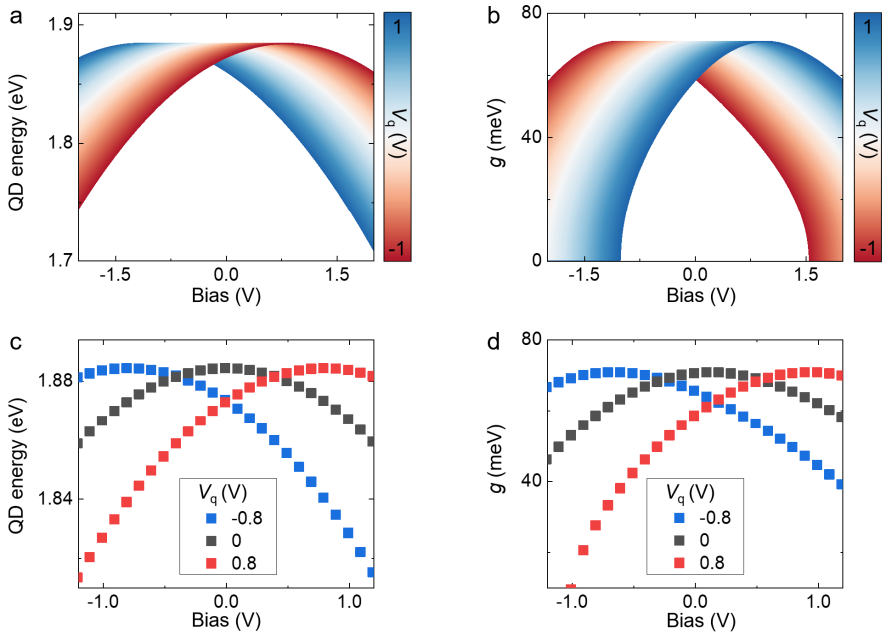

Fig. S20. Estimated Stark shift function with different built-in bias V_q, created by built-in electric field $\vec{E}_q$ (a) and representative Stark shift functions (b). Estimated coupling strength as function of external electric bias with different built-in bias V_q (c) and representative coupling strength functions (d).

To investigate the effect of built-in electric field $\vec{E}_q$ on electrically controlling plexcitonic states, we theoretically estimate the Stark shift and coupling strength as a function of external electric field $\vec{E}_{ext}$ with different built-in bias V_q. Based on the experimentally obtained Stark shift and coupling strength function (Fig. 2b in the main text), exhibiting near quadratic behavior, i.e., $V_q \approx 0$, we gradually change the built-in bias V_q and observe corresponding change in Stark shift and coupling strength function, as shown in Fig. S20a-b. Fig. S20c shows the Stark shift function with negative (V_q = -0.8 V), zero (V_q = 0 V), and positive (V_q = 0.8 V) built-in bias. With center-shifted quadratic function, the QD energy can be either increased or decreased with external electric field. Fig. S20d demonstrate the coupling strength function with negative (V_q = -0.8 V), zero (V_q = 0 V), and positive (V_q = 0.8 V) built-in bias. Likewise, the coupling strength can be bidirectionally tuned with external electric field. Specifically, with the positive built-in bias, the coupling strength is an increasing function of external electric field whereas negative built-in bias causes decreasing function.

S21. Plexciton energies with applying external electric field.

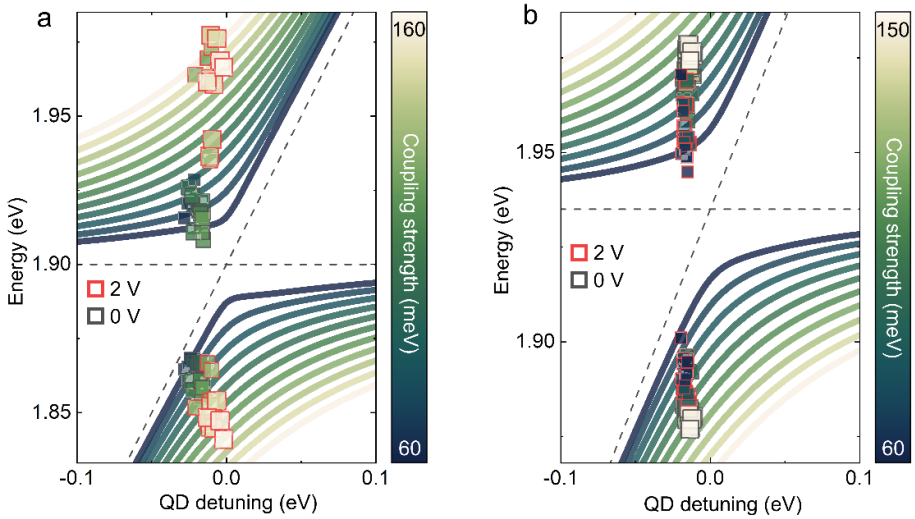

Fig. S21. Polariton energies as function of extracted detuning value, derived from switching TEPL spectra of Fig. 1f (Fig. S21a) and j (Fig. S21b) in main text.

References

[1] Park, K.-D., Jiang, T., Clark, G., Xu, X. and Raschke, M. B. Tip-enhanced strong coupling spectroscopy, imaging, and control of a single quantum emitter. *Sci. Adv*. **5**, eaav5931 (2019).

[2] Flatté, M. E., A. A. Kornyshev, and M. Urbakh. Giant Stark effect in quantum dots at liquid/liquid interfaces: A new option for tunable optical filters. *Proc. Natl. Acad. Sci. U.S.A.* **105**, 18212 (2008).

[3] Li, J. Y., L. Zhang, and Stephen D. Electric energy density of dielectric nanocomposites. *Appl. Phys. Lett.* **90**, 132901 (2007).

[4] Bouhelier, A., Bachelot, R., Lerondel, G., Kostcheev, S., Royer, P., and Wiederrecht, G. P. Surface plasmon characteristics of tunable photoluminescence in single gold nanorods. *Phys. Rev. Lett.* **95**, 267405 (2005)

[5] Mooradian, A. Photoluminescence of metals. *Phys. Rev. Lett.* **22**, 185 (1969)

[6] Mohamed, M. B., Volkov, V., Link, S., and El-Sayed, M. A. The lightning gold nanorods: fluorescence enhancement of over a million compared to the gold metal. *Chem. Phys. Lett.* **317**, 517 (2000)

[7] Kravtsov, V., Berweger, S., Atkin, J. M., and Raschke, M. B. Control of plasmon emission and dynamics at the transition from classical to quantum coupling. *Nano Lett.* **14**, 5270 (2014)

[8] Ekimov, A. I., Efros, A. L., Shubina, T. V., and Skvortzov, A. P. Quantum-size stark effect in semiconductor microcrystals. *J. Lumin.* **46**. 97-100 (1990).

[9] Efros, A. L., Rosen, M., Kuno, M., Nirmal, M., Norris, D. J, and Bawendi, M. G. Band-edge exciton in quantum dots of semiconductors with a degenerate valence band: Dark and bright exciton states. *Phys. Rev B* **54**, 4843-4856 (1996).

[10] Efros, A. L. *Semiconductor and Metal Nanocrystals: Synthesis and Electronic and Optical Properties edited by V. I. Klimov*, (CRC, 2003).

[11] Sercel, P. C., and Efros, A. L. Band-Edge Exciton in CdSe and Other II–VI and III–V Compound Semiconductor Nanocrystals− Revisited. *Nano Lett*. **18,** 4061-4068 (2018).

[12] Efros, A. L. Interband absorption of light in a semiconductor sphere. *Sov. Phys*. *Semicond*. **16**, 772 (1982).

[13] Ekimov, A. I., *et al*. Absorption and intensity-dependent photoluminescence measurements on CdSe quantum dots: assignment of the first electronic transitions. *J. Opt. Soc. Am. B* **10**, 100-107 (1993).

[14] Grigoryan, G. B., Rodina, A. V., and Efros, A. L. Excitons and biexcitons in quantum-well semiconductor microcrystals dispersed in an insulating glassy matrix. *Sov. Phys. Solid state* **32**. 2037-2042 (1990).

[15] Wen, G. W., Lin, Y. J., Jiang, H. X., and Chen, Z. Quantum-confined Stark effects in semiconductor quantum dots. *Phys. Rev. B.* **52**, 5913 (1995).

[16] Chen, Y., Vela, J., Htoon, H., Casson, J. L., Werder, D. J., Bussian, D. A., Klimov, V. I., and Hollingsworth, J. A., Giant multishell CdSe nanocrystal quantum dots with suppressed blinking. *J. Am. Chem. Soc.* **130**, 5026 (2008).

[17] Lim, J., Jeong, B. G., Park, M., Kim, J. K., Pietryga, J. M., Park, Y. S., Klimov, V. I., Lee, C., Lee, D. C., and Bae, W. K., Influence of shell thickness on the performance of light-emitting devices based on CdSe/$Zn_{1-x}Cd_xS$ core/shell heterostructured quantum dots. *Adv. Mater. 26*, 8034 (2014).